CTU Journal of Innovation and Sustainable Development
ISSN 2588-1418 | e-ISSN 2815-6412

DOI:10.22144/ctujoisd.2025.046

Adaptive inner-loop pressure regulation using an RBF-tuned PID for position accuracy and disturbance rejection in PAM systems

Vinh-Phuc Tran[1,2,3], Hoang-Linh Vo[1,2], Nhut-Thanh Tran[1], Chi-Ngon Nguyen[1], and Chanh-Nghiem Nguyen[1,2*]

[1]*Faculty of Automation Engineering, Can Tho University, Viet Nam*

[2]*Automation Laboratory, Can Tho University, Viet Nam*

[3]*Faculty of Mechanical Engineering Technology, Vinh Long University of Technology Education, Viet Nam*

**Corresponding author (ncnghiem@ctu.edu.vn)*

Article info.

Received 23 Feb 2025
Revised 6 Jun 2025
Accepted 30 Jul 2025

Keywords

Adaptive control, disturbance rejection, dual-loop control scheme, pneumatic artificial muscle, pressure control, RBF neural network, real-time PID tuning

ABSTRACT

This study investigates the impact of inner-loop pressure regulation on the dynamic performance of pneumatic artificial muscle (PAM) systems using a dual-loop control architecture. Three pressure control strategies – Proportional-Integral (PI), Proportional-Integral-Derivative (PID), and Radial Basis Function neural network-tuned PID (RBF-PID) – are experimentally evaluated in terms of tracking accuracy, transient response, and disturbance rejection. Results show that the RBF-PID controller achieves the highest accuracy of pressure tracking , with a root-mean-square error (RMSE) of 0.067 bar under a modulated sinusoidal input, outperforming PID (0.088 bar) and PI (0.094 bar) controllers. In position control tasks, all dual-loop configurations offer improved stability compared to the single-loop setup. The RBF-PID controller further enhances performance, achieving a settling time of 3.04 seconds, zero overshoot, and the shortest recovery time of 2.73 seconds under a 10-kg load disturbance. Although the performance gap between PI and PID remains modest, suggesting PI remains a practical solution for resource-constrained applications, the RBF-PID controller provides significant benefits in adaptability and robustness. These findings underscore the importance of adaptive pressure regulation in improving the tracking accuracy and resilience of PAM-based actuators. The choice of control strategy should therefore be guided by the specific application context, balancing control performance with computational and hardware constraints.

1. INTRODUCTION

Pneumatic Artificial Muscles (PAMs) have gained significant attention in soft robotics and assistive technologies due to their high compliance, lightweight structure, and excellent power-to-weight ratio (Plettenburg, 2005; Kalita et al., 2022). Their practicality has been demonstrated in real-world applications, such as lower-limb rehabilitation robots. For example, Tsai and Chiang (Tsai & Chiang, 2023) developed a system using a single PAM and torsion spring to achieve two-degree-of-freedom motion. Structurally, a PAM consists of an internal elastic bladder surrounded by a braided mesh. When pressurized, the bladder expands radially and contracts axially, generating

tensile force; when depressurized, it returns to its original length (Zabihollah et al., 2024). This unique mechanism enables smooth, biomimetic motion but also introduces substantial challenges in control. The compressibility of air, nonlinear pressure–length relationships, and system hysteresis lead to significant nonlinearity and dynamic delay, which complicate both force and position control (Jamian et al., 2020; Shakiba et al., 2021; Al Saaideh & Al Janaideh, 2022; Vo & Ahn, 2022).

To address these complexities, many studies have adopted dual-loop control architectures, in which the inner loop regulates air pressure, while the outer loop controls the position or force of the actuator (Robinson et al., 2016; Lin et al., 2021). This structure is conceptually advantageous, as it decouples fast pneumatic dynamics from slower mechanical responses, potentially improving system stability and responsiveness. For example, (Tran et al., 2023) demonstrated that a dual-loop controller incorporating a Proportional-Integral (PI) pressure regulator achieved a settling time of 0.5 seconds for step inputs and 1.5 seconds for square-wave signals, with an overshoot of only 0.3 bar during position control tests under a 25 kg load and 65% stroke (23 mm). However, most previous research has applied this dual-loop strategy without systematically comparing it to position-only control, and without quantitatively evaluating the benefit of inner-loop pressure control. Furthermore, few studies assess how pressure regulation affects robustness when the system is exposed to external disturbances, such as load variations or input noise (Takosoglu, 2020). This presents a clear gap in the literature that must be addressed to validate the true effectiveness of dual-loop architectures in practical PAM applications.

Beyond dual-loop control, accurate pressure regulation is also crucial for other advanced PAM control strategies. In particular, model-based methods such as hysteresis inversion or feedforward compensation depend heavily on precise pressure tracking to ensure reliable actuator behavior. For example, (Zang et al., 2017) employed a modified Prandtl–Ishlinskii model for position control of a single PAM with better performance compared with earlier works (Choi et al., 2006; Liu et al., 2015). However, the effectiveness of such hysteresis modeling hinges on the assumption that pressure is well-regulated. Similarly, Zhang et al. (2024) also found that stable pressure dynamics are critical for direct inverse hysteresis compensation strategies with fuzzy sliding-mode controllers in controlling PAM-based humanoid robot manipulators. Therefore, pressure control is not merely an auxiliary task but a critical requirement in a wide range of PAM control paradigms.

Addressing this issue requires a closer look at the pressure control strategies employed in the inner loop. Several methods have been explored for regulating air pressure in PAMs. The PI controller remains widely used due to its simplicity and low computational demands (Arun Jayakar & Tamilselvan, 2019; Zorro et al., 2022). However, in systems with strong nonlinearities and delays, PI control often results in overshoot, long settling time, and poor disturbance rejection (Massoud & Libby, 2024). To overcome these limitations, advanced control techniques such as fuzzy logic, model predictive control, and gain scheduling have been proposed (Ruan & Yang, 2020; Hou et al., 2022; Flores et al., 2023). Although not applied to PAM systems, similar research has explored the use of adaptive learning methods; for example, Radial Basis Function Neural Network-tuned PID (RBF-PID) controllers for real-time PID tuning in other dynamic systems, showing promising results (Wang et al., 2022). This approach dynamically adjusts the Proportional-Integral-Derivative (PID) parameters based on real-time error dynamics and system states, allowing improved tracking accuracy and adaptability. In one study, RBF-PID control applied to a robotic arm achieved 0.01% overshoot and reduced settling time from 2.2 s (obtained with a conventional PID controller) to just 1 s, even under noise. In another study about DC motor control, it halved the settling time (0.65 s vs. 1.35 s) and eliminated overshoot under parameter variations (Wang et al., 2022). However, there is limited evidence directly comparing their performance to PI controllers in PAM pressure control applications, particularly under disturbances or when integrated into full position control systems (Massoud & Libby, 2024).

This study aims to evaluate systematically the role and effectiveness of inner-loop pressure control in PAM systems by addressing two key objectives:

1. The first objective of this study is to compare the performance of three pressure control strategies: the discrete PI controller, the discrete PID controller, and the adaptive discrete RBF-PID controller. All controllers are evaluated under identical operating conditions, with pressure tracking accuracy assessed using the RMSE metric

during both contraction and extension phases of the PAM actuator.

2. The second objective of this study is to investigate the influence of inner-loop pressure regulation on outer-loop position control performance. This is accomplished by analyzing and comparing the system's dynamic behavior under three distinct control configurations: (1) position control without any form of pressure regulation, (2) position control incorporating a discrete PI controller in the inner pressure loop, and (3) position control employing an adaptive discrete RBF-PID controller for inner-loop pressure control. By evaluating these configurations under both nominal and disturbed conditions, the study aims to quantify the impact of pressure control quality on the overall precision and robustness of the PAM system. For each configuration, we evaluate performance using percentage overshoot (POT), rise time, and settling time, both under nominal conditions and with external disturbances, to assess not only control precision but also system robustness.

Through this two-stage approach, the study provides new insights into the interaction between inner- and outer-loop dynamics in PAM-based systems and offers practical guidance for the design of adaptive, disturbance-resilient control strategies in real-world soft robotic applications.

2. MATERIALS AND METHODS

2.1. Experimental setup

Figure 1 presents the experimental setup utilized in this study. A PAM with a diameter of 40 mm and an initial length of 300 mm (FESTO MAS-40-300N) was employed. Displacement measurements were acquired using an Accuracy™ KTC100 position sensor, while internal air pressure was monitored by a Honeywell pressure transducer. A FESTO MPYE 5/3 proportional directional control valve managed the airflow to and from the actuator. The control system and data acquisition were developed in MATLAB/Simulink, operating with a sampling interval of 10 ms. All position and pressure signals were obtained from the physical model and digitized by a Texas Instruments C2000 LaunchPAD, which features a 12-bit analog-to-digital converter.

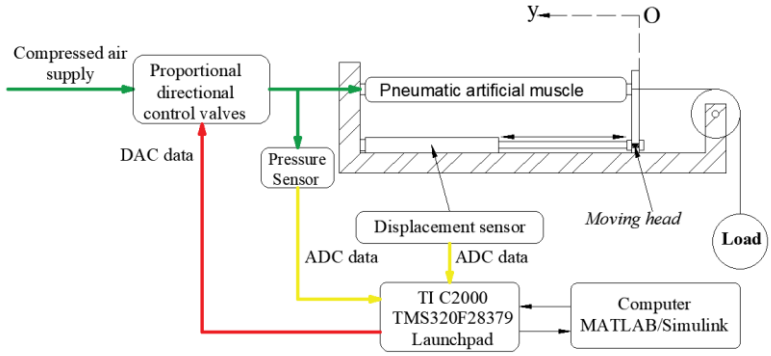

Figure 1. Experiment setup

2.2. Dual-loop control architecture

In this study, the control system is designed based on a dual-loop architecture to leverage the distinct physical and dynamic characteristics of different components in the PAM system. As shown in Figure 2, the architecture consists of:

– *An inner loop controller*: Responsible for regulating the compressed air pressure supplied to the muscle. To confirm the better performance of the proposed discrete RBF-PID controller, conventional discrete PI and PID controllers were also implemented for comparison purposes.

– *An outer loop*: Responsible for the position tracking of the PAM endpoint. In this study, a PID controller was used.

This hierarchical structure separates fast-response pressure regulation from slower position control, thereby improving system stability, simplifying parameter tuning, and enhancing overall performance, as supported by previous research (Tran et al., 2023).

2.3. Position controller in outer-loop

The outer-loop discrete PID controller generates the the outer control signal $u_y(k)$ at discrete time step k as follows:

$$u_y(k) = K_P \cdot e_y(k) + K_I \cdot \sum_{i=0}^{k} e_y(k) \cdot T_s + K_D \cdot \frac{e_y(k) - e_y(k-1)}{T_s} \quad (1)$$

where $e_y(k)$ is the position error at time k and the sampling time is $T_s = 0.01$ s. The proportional, integral, and derivative gains were empirically set as $K_P = 15$, $K_I = 4$, and $K_D = 0.1$, respectively.

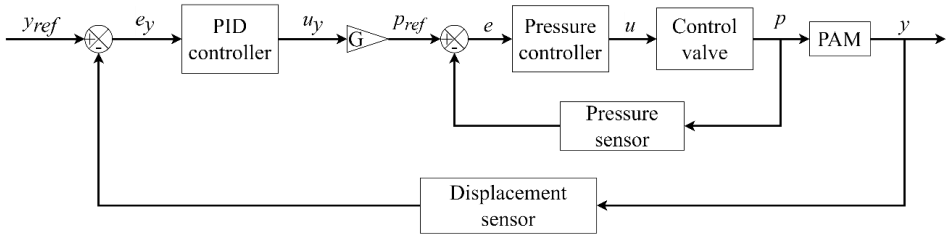

Figure 2. Block diagram of the two-loop control structure

The discrete-time control signal $u_y(k)$ is converted to the reference pressure p_{ref} for the inner pressure-control loop as follows:

$$p_{ref} = G \cdot u_y \quad (2)$$

where $G = 6/84\,(\text{bar/mm})$ is the displacement-to-pressure conversion ratio, experimentally determined based on the fact that the PAM exhibits a contraction of approximately 84 mm in response to the maximum input pressure of 6.0 bar and a load of 15–25 kg.

2.4. Pressure controllers

This study evaluates three pressure controllers, which are PI, PID, and adaptive RBF-PID controllers. The control signal is applied to a proportional valve to regulate airflow within the range of 0–6 bar. The inner pressure control system is a single-input single-output system with the associated signals as follows:

- $p_{ref}(k)$: Reference pressure at time step k,
- $p(k)$: Pneumatic pressure at time step k,
- $e(k) = p_{ref}(k) - p(k)$: Pressure error at time step k,
- $u(k)$: Control signal output at time k.

2.4.1. Pressure control using a PI controller

The output signal of the PI controller is given by:

$$u(k) = u_{PI}(k) = K_{P1} \cdot e(k) + K_{I1} \cdot \sum_{i=0}^{k} e(k) \cdot T_s \quad (3)$$

where K_{P1} and K_{I1} are the proportional and integral gains of the PI controller, respectively. These gains were empirically set as $K_{P1} = 2.2$ and $K_{I1} = 4.6$ to achieve a short settling time, minimal steady-state error, and negligible overshoot.

2.4.2. Pressure control using a PID controller

The PID controller enhances pressure regulation by adding a derivative term to the PI structure. The derivative term predicts future error trends by estimating the rate of change of error, improving responsiveness, and reducing overshoot during sudden reference changes. While effective in improving transient behavior, PID control remains sensitive to noise and tuning complexity in nonlinear systems.

$$u(k) = u_{PID}(k) = K_{P2} \cdot e(k) + K_{I2} \cdot \sum_{i=0}^{k} e_p(i) \cdot T_s + K_{D2} \cdot \frac{e(k) - e(k-1)}{T_s} \quad (4)$$

where K_{P2}, K_{D2}, and K_{I2} are the proportional, derivative, and integral gains of the PID controller, respectively. These gains were also empirically tuned and set to $K_{P2} = 2.0$, $K_{D2} = 0.2$, and $K_{I2} = 4.6$, respectively.

2.4.3. Pressure control using an RBF-PID controller

To enhance control performance for systems with nonlinear characteristics, delays, and dynamic variations, this study employs a discrete PID controller combined with a Radial Basis Function (RBF) neural network, forming an adaptive RBF-PID controller (Figure 3). This control scheme allows real-time tuning of PID parameters, improving control accuracy and adaptability.

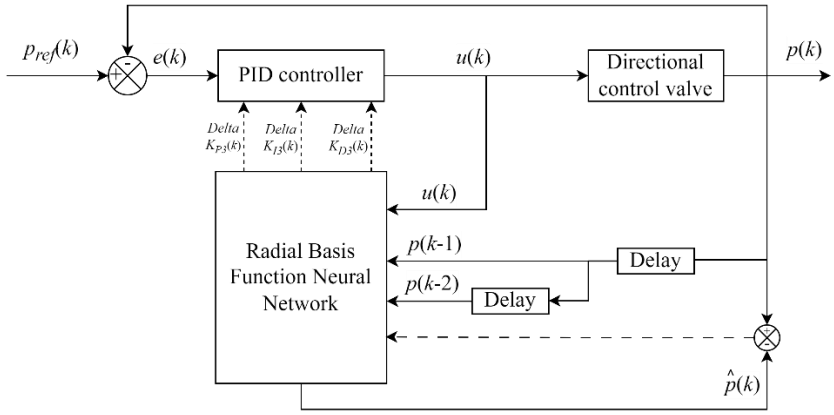

Figure 3. RBF-PID controller structure

The control law of the proposed RBF-PID is formulated similarly to the standard PID structure, as in Eq. (3).

$$\begin{aligned} u(k) &= u_{RBF-PID}(k) \\ &= K_{P3}\cdot e(k) + K_{I3}\cdot \sum_{i=0}^{k} e_p(i)\cdot T_s \\ &\quad + K_{D3}\cdot \frac{e(k)-e(k-1)}{T_s} \end{aligned} \tag{5}$$

However, the PID gains are continuously updated by the RBF neural network to minimize the cost function:

$$E(k) = \frac{1}{2}\left[e(k)\right]^2 \tag{6}$$

where

$$e(k) = p_{ref}(k) - p(k) \tag{7}$$

Using a gradient descent learning mechanism, the proportional, integral, and derivative gains are updated as follows:

$$K_{P3}(k+1) = K_{P3}(k) + \Delta K_{P3}(k) \tag{8}$$

$$K_{I3}(k+1) = K_{I3}(k) + \Delta K_{I3}(k) \tag{9}$$

$$K_{D3}(k+1) = K_{D3}(k) + \Delta K_{D3}(k) \tag{10}$$

After each time step k, the gain updates are respectively computed as:

$$\begin{aligned} \Delta K_{P3}(k) &= -\eta \frac{\partial E(k)}{\partial K_{P3}(k)} \\ &= -\eta \frac{\partial E(k)}{\partial p(k)} \frac{\partial p(k)}{\partial u(k)} \frac{\partial u(k)}{\partial K_{P3}(k)} \\ &= \eta e(k) \frac{\partial p(k)}{\partial u(k)} \frac{\partial u(k)}{\partial K_{P3}(k)} \end{aligned} \tag{11}$$

$$\begin{aligned} \Delta K_{I3}(k) &= -\eta \frac{\partial E(k)}{\partial K_{I3}(k)} \\ &= -\eta \frac{\partial E(k)}{\partial p(k)} \frac{\partial p(k)}{\partial u(k)} \frac{\partial u(k)}{\partial K_{I3}(k)} \\ &= \eta e(k) \frac{\partial p(k)}{\partial u(k)} \frac{\partial u(k)}{\partial K_{I3}(k)} \end{aligned} \tag{12}$$

$$\begin{aligned} \Delta K_{D3}(k) &= -\eta \frac{\partial E(k)}{\partial K_{D3}(k)} \\ &= -\eta \frac{\partial E(k)}{\partial p(k)} \frac{\partial p(k)}{\partial u(k)} \frac{\partial u(k)}{\partial K_{D3}(k)} \\ &= \eta e(k) \frac{\partial p(k)}{\partial u(k)} \frac{\partial u(k)}{\partial K_{D3}(k)} \end{aligned} \tag{13}$$

where η is the learning rate; $\frac{\partial p(k)}{\partial u(k)}$ is the Jacobian of the plant, estimated by the RBF network; and the partial derivatives of the discrete-time control signal $u(k)$ with respect to K_{P3}, K_{I3}, and K_{D3} are computed as follows:

$$\frac{\partial u(k)}{\partial K_{P3}(k)} = e(k) \tag{14}$$

$$\frac{\partial u(k)}{\partial K_{I3}(k)} = \left(\sum_{i=0}^{k} e(k)\cdot T_s\right) \tag{15}$$

$$\frac{\partial u(k)}{\partial K_{D3}(k)} = \frac{e(k)-e(k-1)}{T_s} \tag{16}$$

Figure 4 shows the structure of the RBF network used for the discrete RBF-PID controller. This network was designed based on previous reports (Jiang-Jiang et al., 2008; Hien et al., 2018). It has 1

hidden layer with 5 neurons. It receives the current control signal $u(k)$ and two past pressure values $p(k-1)$ and $p(k-2)$, forming the input vector as follows:

$$\mathbf{x}(k) = \begin{bmatrix} u(k) & p(k-1) & p(k-2) \end{bmatrix}^T \quad (17)$$

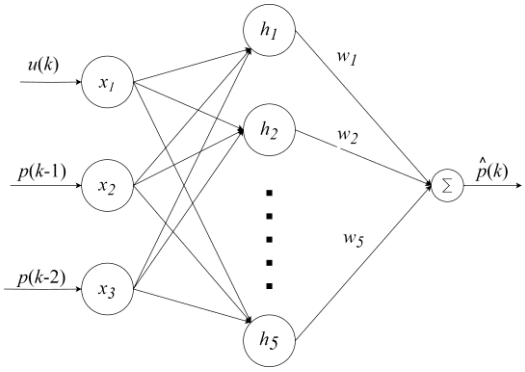

Figure 4. RBF network structure

The network output is computed as:

$$\hat{p} = \sum_{j=1}^{m} w_j \cdot h_j \quad (18)$$

where w_j is the connection weight between the output neuron and the hidden neuron j, whose activation function is calculated as

$$h_j = \exp\left(-\frac{\left\| \mathbf{x} - \mathbf{c}_j \right\|^2}{2b_j^2} \right) \quad (19)$$

where b_j and $\mathbf{c}_j$ are the width (spread) of the Gaussian activation function and the center vector of neuron j, respectively, and $\|\bullet\|$ denotes the Euclidean norm operation.

The Jacobian for online update of PID gains is calculated from the network output as:

$$\frac{\partial p}{\partial u} \approx \frac{\partial \hat{p}}{\partial u} = \sum_{j=1}^{m} w_j h_j \frac{c_{1j} - x_1}{b_j^2} \quad (20)$$

where c_{1j} and x_1 are the first elements of $\mathbf{c}_j$ and $\mathbf{x}$, respectively. Therefore,

$$\frac{\partial p}{\partial u} = \sum_{j=1}^{m} w_j h_j \frac{c_{1j} - u}{b_j^2} \quad (21)$$

For Eq. (19) to hold, the RBF network parameters should be updated to minimize the estimation error:

$$E_{RBF}(k) = \frac{1}{2}\left[e_{RBF}(k) \right]^2 \quad (22)$$

where

$$e_{RBF}(k) = p(k) - \hat{p}(k) \quad (23)$$

In this study, the RBF network is trained with gradient descent and momentum. The connection weights, the widths of the Gaussian functions, and the centers of the hidden neurons are adjusted as follows:

$$w_j(k+1) = w_j(k) + \Delta w_j(k) \quad (24)$$

$$b_j(k+1) = b_j(k) + \Delta b_j(k) \quad (25)$$

$$\mathbf{c}_j(k+1) = \mathbf{c}_j(k) + \Delta \mathbf{c}_j(k) \quad (26)$$

where

$$\begin{aligned} \Delta w_j(k) &= -\eta \frac{\partial E_{RBF}(k)}{\partial w_j(k)} \\ &\quad + \alpha \left(w_j(k) - w_j(k-1) \right) \\ &= \eta e_{RBF}(k) h_j(k) \\ &\quad + \alpha \left(w_j(k) - w_j(k-1) \right) \end{aligned} \quad (27)$$

$$\begin{aligned} \Delta b_j(k) &= -\eta \frac{\partial E_{RBF}(k)}{\partial b_j(k)} \\ &\quad + \alpha \left(b_j(k) - b_j(k-1) \right) \\ &= \eta e_{RBF}(k) w_j(k) h_j(k) \frac{\left\| \mathbf{x}(k) - \mathbf{c}_j(k) \right\|^2}{b_j^{\,3}(k)} \\ &\quad + \alpha \left(b_j(k) - b_j(k-1) \right) \end{aligned} \quad (28)$$

$$\begin{aligned} \Delta \mathbf{c}_j(k) &= -\eta \frac{\partial E_{RBF}(k)}{\partial \mathbf{c}_j(k)} \\ &\quad + \alpha \left(\mathbf{c}_j(k) - \mathbf{c}_j(k-1) \right) \\ &= \eta e_{RBF}(k) w_j(k) h_j(k) \frac{\mathbf{x}(k) - \mathbf{c}_j(k)}{b_j^{\,2}(k)} \\ &\quad + \alpha \left(\mathbf{c}_j(k) - \mathbf{c}_j(k-1) \right) \end{aligned} \quad (29)$$

The learning rate and momentum factor were chosen as $\eta = 0.01$ and $\alpha = 0.9$, respectively. The initial values of the PID gains are selected based on the baseline performance of the conventional PID controller as $K_{P3}(0) = 3.2$, $K_{D3}(0) = 0.01$,

$K_{I3}(0) = 2.0$. The width parameters were initially set at $b_j = 3$. The center matrix was initialized at

$$C = \begin{bmatrix} \mathbf{c}_1 & \mathbf{c}_2 & \mathbf{c}_3 & \mathbf{c}_4 & \mathbf{c}_5 \end{bmatrix} = \begin{bmatrix} 0 & 1.5 & 3 & 4.5 & 6 \\ 0 & 1.5 & 3 & 4.5 & 6 \\ 0 & 1.5 & 3 & 4.5 & 6 \end{bmatrix}$$

3. RESULTS AND DISCUSSION

3.1. Overall performance of the investigated pressure controllers

3.1.1. Experiment 1: Pressure regulation with simple reference signals

To evaluate the performance of the proposed RBF-PID controller, two distinct reference signals – a damped triangular waveform and a damped sinusoidal waveform – were used to compare against conventional discrete PI and PID controllers. The damped triangular signal, characterized by sharp transitions and a linearly decreasing amplitude, posed a challenge in abrupt signal variations (P_{ref} signal in Figure 5). In contrast, the damped sinusoidal signal provided a smoother and more gradual variation (P_{ref} signal in Figure 6).

Figures 5 and 6 show the pressure tracking results for the three controllers. All controllers generally followed the reference signals, but the discrete RBF-PID controller achieved higher accuracy, particularly for the sinusoidal signal. The discrete RBF-PID achieved a lower RMSE of 0.069 bar, compared to 0.094 bar for PI and 0.088 bar for PID controllers (Table 1).

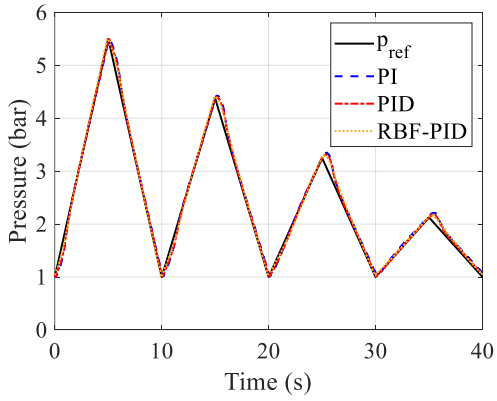

Figure 5. Tracking performance with a damped triangular reference

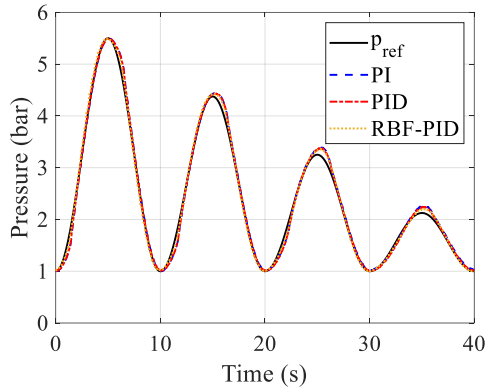

Figure 6. Tracking performance with a damped sinusoidal reference

Table 1. RMSE for damped triangular and sinusoidal signals

Discrete controller	Damped triangular signal (bar)	Damped sinusoidal signal (bar)
PI	0.107	0.094
PID	0.089	0.088
RBF-PID	0.086	0.069

3.1.2. Experiment 2: Pressure regulation with more complicated reference signals

To further assess the robustness of the proposed controller, a second experiment employed more complex and dynamic reference signals, designed to simulate realistic pressure fluctuations. These signals featured varying amplitudes and non-uniform decay patterns to challenge the adaptability of each controller. For comparison purposes, both reference signals had amplitudes ranging from 1.0 to 5.5 bar, consistent with those in Experiment 1.

The first signal was a triangular waveform with varying peak amplitudes (P_{ref} signal in Figure 7), designed to introduce asymmetry and abrupt slope changes. The second signal was a modulated sinusoidal waveform with irregular amplitude decay (P_{ref} signal in Figure 8), simulating oscillatory yet non-uniform pressure demands often encountered in real-world scenarios.

As shown in Figures 7 and 8, all controllers maintained acceptable tracking. However, the discrete RBF-PID consistently showed closer adherence to the reference signals, particularly during abrupt changes. This was also reflected in RMSE values (Table 2), where the discrete RBF-PID achieved 0.088 bar and 0.067 bar in tracking the triangular and modulated sinusoidal signals,

respectively. These results confirm that the discrete RBF-PID controller offers improved tracking accuracy, especially for signals with nonstationary or irregular characteristics.

As highlighted in Figures 8 and 9, all controllers exhibited sufficient tracking performance, validating the necessity of incorporating an inner-loop controller - even a simple PI - for effective pressure regulation. Nonetheless, the discrete RBF-PID controller again outperformed both the PI and PID controllers, showing smaller deviations around rapid waveform changes and yielding lower RMSE values (Table 2). These findings confirm the advantage of the RBF-enhanced PID design in managing nonlinear and dynamic pneumatic system behavior.

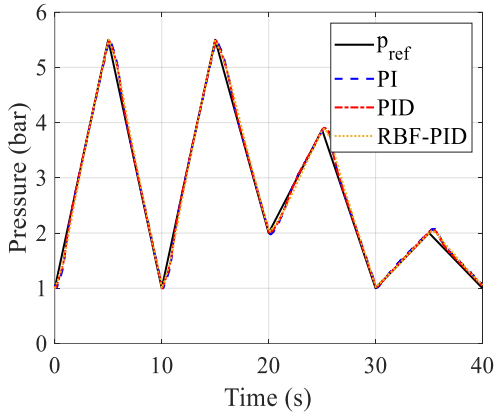

Figure 7. Tracking with a triangular signal of variable amplitude

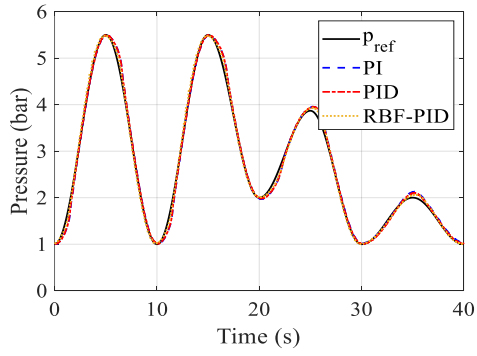

Figure 8. Tracking with a modulated sinusoidal signal

Table 2. RMSE for complex reference signals

Discrete controller	Variable triangular signal (bar)	Modulated sinusoidal signal (bar)
PI	0.111	0.094
PID	0.104	0.088
RBF-PID	0.088	0.067

3.2. Performance of PAM position control with and without load disturbance

Given that this study primarily focuses on the design of the discrete RBF-PID controller for pressure regulation, a discrete PID controller was employed for PAM position control across all tested configurations. System performance was evaluated under four different pressure control schemes using 45-mm step inputs across two intervals:

i) 0–9 seconds: Evaluation of transient characteristics.

ii) 9–20 seconds: Assessment of response under external load disturbance, introduced by manually applying a 10-kg mass on the actuator.

The four tested pressure control schemes were:

1. Position-only control (without pressure feedback),

2. Dual-loop control with discrete PI pressure regulation,

3. Dual-loop control with discrete PID pressure regulation,

4. Dual-loop control with discrete RBF-PID pressure regulation.

Four key performance metrics, which are rise time, settling time, and percent overshoot (POT), are summarized in Table 3.

Table 3. Step response characteristics under different pressure control schemes

Discrete controller	Rise time (s)	Settling time (s)	Percent of overshoot (%)
None	0.06	7.73	6.32
PI	1.36	7.51	2.82
PID	1.37	7.50	2.73
RBF-PID	1.40	3.04	0.00

3.2.1. Characteristics of the step responses

As shown in Figure 9, omitting pressure feedback led to the shortest rise time (0.06 s), but poor damping and significant overshoot (6.32%) due to the unmitigated nonlinear dynamics of pneumatic actuation.

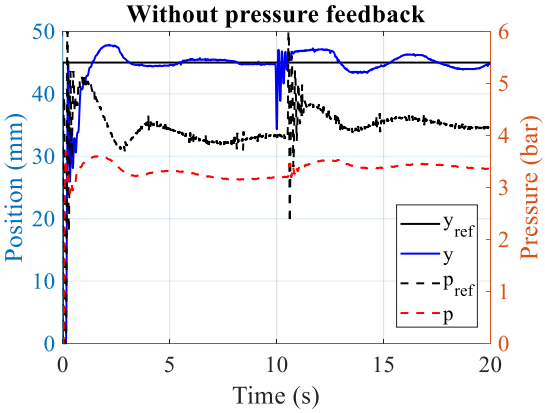

Figure 9. Position and pressure responses using control without pressure feedback

In contrast, all dual-loop configurations with pressure feedback (PI, PID, and RBF-PID) yielded slower but more stable responses, with reduced overshoot. The PI and PID controllers decreased the POT by more than 50% compared to the no-feedback case. However, they did not substantially improve the settling time. Notably, the RBF-PID controller achieved complete overshoot suppression and reduced the settling time by nearly 60% (from 7.73 s to 3.04 s), as shown in Figures 10–12. These results highlight the benefit of adaptive gain tuning via the RBF network in effectively compensating for transient nonlinearities and pressure fluctuations.

3.2.2. System responses to load disturbances

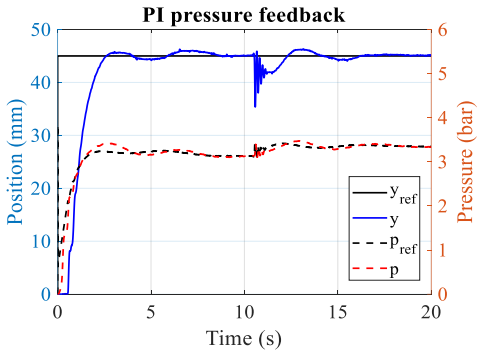

Figure 10. Position and pressure responses using dual-loop control with PI pressure regulation

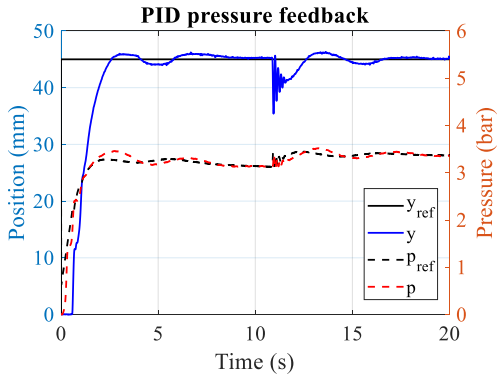

Figure 11. Position and pressure responses using dual-loop control with PID pressure regulation

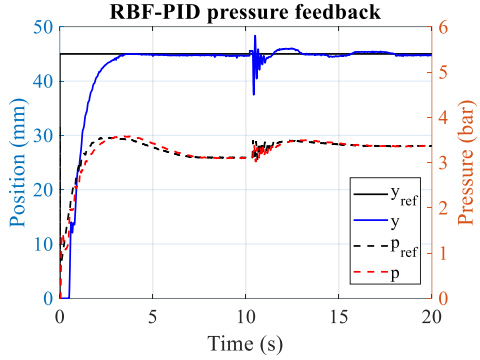

Figure 12. Position and pressure responses using dual-loop control with RBF-PID pressure regulation

To assess robustness, a 10-kg external load was applied at steady state, causing a sudden PAM displacement of approximately 7.5 mm in all cases (Figure 12). Recovery time – the duration required to return to the reference position – varied significantly across controllers (Table 4).

Table 4. Effect of pressure control on recovery time under external load disturbance

Discrete controller	Disturbance recovery time (s)
None	9.95
PI	5.76
PID	5.68
RBF-PID	2.73

Without pressure regulation, recovery took approximately 9.95 s. Both PI and PID controllers reduced this to ~5.7 s (a 43% improvement). Impressively, the discrete RBF-PID controller enabled the fastest recovery at just 2.73 s. This result confirms both the advantage of dual-loop control in load disturbance scenarios and the superior

adaptability of the discrete RBF-PID controller, which effectively compensates for dynamic variations and nonlinear disturbances in real time.

The effectiveness of real-time PID gain adaptation via the RBF network is further illustrated in Figure 13, which shows the dynamic adjustments of the PID gains during the control process. Notably, significant gain updates occur around the period of 10–14 seconds, coinciding with the period of external load disturbance. This adaptive response enables the controller to compensate rapidly for the introduced disturbance, contributing to faster recovery and improved overall stability. The ability to modify control gains in real time allows the discrete RBF-PID controller to maintain high tracking accuracy and robust disturbance rejection, confirming the advantage of using a learning-based approach in pneumatic control applications.

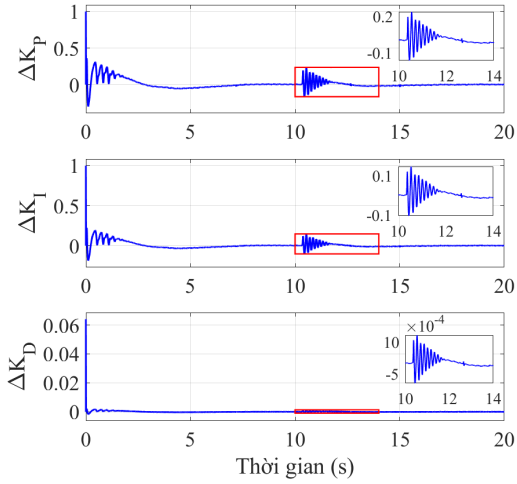

Figure 13. PID gain updates with RBF-PID pressure regulation

4. CONCLUSION

Inner-loop pressure regulation plays a critical role in shaping the dynamic response of pneumatic artificial muscle (PAM) systems. Of the three evaluated strategies, the proposed adaptive discrete RBF-PID controller consistently demonstrated superior pressure tracking performance. It achieved the lowest root-mean-square error (RMSE) of 0.067 bar under a modulated sinusoidal reference, outperforming the conventional discrete PID and discrete PI controllers, which recorded RMSEs of 0.088 bar and 0.094 bar, respectively. However, the performance difference between discrete PI and discrete PID controllers remained relatively small across all test cases, particularly under noisy or irregular conditions. This suggests that, for applications with limited computational resources or operating in uncertain environments, the discrete PI controller remains a practical and robust choice, offering reliable performance with minimal implementation complexity.

In position control tasks, the benefits of adaptive pressure regulation became even more apparent. All dual-loop configurations outperformed the single-loop approach by enhancing system stability and transient behavior. Among them, the RBF-PID controller achieved the best overall performance, with a settling time of 3.04 seconds, zero overshoot, and the fastest recovery from external disturbances, returning to the reference position in just 2.73 seconds after a 10-kg load perturbation. These results were supported by the observed real-time adjustments of PID gains, which confirmed the controller's ability to adapt to dynamic changes and maintain stability under varying conditions.

However, the improved performance of the discrete RBF-PID controller comes at the cost of increased computational demand. Its real-time learning and adaptive gain tuning require higher processing capacity, which may pose challenges for deployment on low-cost or embedded platforms, especially when paired with advanced outer-loop control strategies.

In conclusion, the choice of control architecture should be guided by the specific application context, hardware limitations, and performance requirements. While the discrete RBF-PID controller is well-suited for precision-critical and adaptive systems, simpler approaches such as discrete PI control continue to offer a valuable balance between performance and practicality in resource-constrained scenarios.

CONFLICT OF INTEREST

The authors declare that they have no known conflict of interest.

REFERENCES

Al Saaideh, M., & Al Janaideh, M. (2022). On Prandtl–Ishlinskii Hysteresis Modeling of a Loaded Pneumatic Artificial Muscle. *ASME Letters in Dynamic Systems and Control*, *2*(3), 1–12. https://doi.org/10.1115/1.4054779

Arun Jayakar, S., & Tamilselvan, G. M. (2019). Mathematical modelling and robust PID controller design for compressed air pressure control process. *Applied Mathematics and Information Sciences*, *13*(4), 561–567. https://doi.org/10.18576/amis/130407

Choi, T., Lee, J., & Lee, J. (2006). Control of Artificial Pneumatic Muscle for Robot Application. *2006 IEEE/RSJ International Conference on Intelligent Robots and Systems*, 4896–4901. https://doi.org/10.1109/IROS.2006.282447

Flores, T. K. S., Villanueva, J. M. M., & Gomes, H. P. (2023). Fuzzy Pressure Control: A Novel Approach to Optimizing Energy Efficiency in Series-Parallel Pumping Systems. *Automation*, *4*(1), 11–28. https://doi.org/10.3390/automation4010002

Hien, H. T., Dung, N. H., & Vu, H. M. (2018). Radial basic function based PID controller. *Can Tho University, Journal of Science*, *54*(7), 9. https://doi.org/10.22144/ctu.jvn.2018.118

Hou, Q., Ma, L., Wang, H., & Ding, S. (2022). Fuzzy Disturbance Observer Design for a Class of Nonlinear SISO Systems. *International Journal of Fuzzy Systems*, *24*(1), 147–158. https://doi.org/10.1007/s40815-021-01116-8

Jamian, S., Salim, S. N. S., Kamarudin, M. N., Zainon, M., Syed Mohamad, M. S., Abdullah, L., & Hanafiah, M. A. M. (2020). Review on controller design in pneumatic actuator drive system. *Telkomnika (Telecommunication Computing Electronics and Control)*, *18*(1), 332–342. https://doi.org/10.12928/TELKOMNIKA.V18I1.12626

Jiang-Jiang W., Chun-Fa Z., & You-Yin J. (2008). Self-adaptive RBF neural network PID control in exhaust temperature of micro gas turbine. *2008 International Conference on Machine Learning and Cybernetics*, 2131–2136. https://doi.org/10.1109/ICMLC.2008.4620758

Kalita, B., Leonessa, A., & Dwivedy, S. K. (2022). A Review on the Development of Pneumatic Artificial Muscle Actuators: Force Model and Application. *Actuators*, *11*(10), 288. https://doi.org/10.3390/act11100288

Lin, C.-J. J., Sie, T.-Y. Y., Chu, W.-L. L., Yau, H.-T. T., & Ding, C.-H. H. (2021). Tracking Control of Pneumatic Artificial Muscle-Activated Robot Arm Based on Sliding-Mode Control. *Actuators*, *10*(3), 66. https://doi.org/10.3390/act10030066

Liu, Y., Zang, X., Liu, X., & Wang, L. (2015). Design of a biped robot actuated by pneumatic artificial muscles. *Bio-Medical Materials and Engineering*, *26*(1_suppl), S757–S766. https://doi.org/10.3233/BME-151367

Massoud, M. M., & Libby, J. (2024). Comparative Analysis of Evolutionary Algorithms for PID Controller Optimization in Pneumatic Soft Robotic Systems: A Simulation and Experimental Study. *IEEE Access*, *12*(September), 151749–151769. https://doi.org/10.1109/ACCESS.2024.3480834

Plettenburg, D. H. (2005). Pneumatic actuators: a comparison of energy-to-mass ratio's. *9th International Conference on Rehabilitation Robotics, 2005. ICORR 2005.*, *2005*, 545–549. https://doi.org/10.1109/ICORR.2005.1502022

Qi, W., Yang, B., & Chao, Y. (2022). Research on Hydraulic Servo Valve Control Based on Fuzzy RBF. *Journal of Physics: Conference Series*, *2417*(1), 0–10. https://doi.org/10.1088/1742-6596/2417/1/012029

Ren, H. P., Jiao, S. S., Li, J., & Deng, Y. (2022). Adaptive neural network control of pneumatic servo system considering state constraints. *Mechanical Systems and Signal Processing*, *162*(May 2021), 107979. https://doi.org/10.1016/j.ymssp.2021.107979

Robinson, R. M., Kothera, C. S., Sanner, R. M., & Wereley, N. M. (2016). Nonlinear Control of Robotic Manipulators Driven by Pneumatic Artificial Muscles. *IEEE/ASME Transactions on Mechatronics*, *21*(1), 55–68. https://doi.org/10.1109/TMECH.2015.2483520

Ruan, Z., & Yang, Q. (2020). Adaptive fuzzy output-constrained control of uncertain MISO nonlinear systems with actuator faults. *IFAC-PapersOnLine*, *53*(2), 13739–13744. https://doi.org/10.1016/j.ifacol.2020.12.879

Shakiba, S., Ourak, M., Poorten, E. Vander, Ayati, M., & Yousefi-Koma, A. (2021). Modeling and compensation of asymmetric rate-dependent hysteresis of a miniature pneumatic artificial muscle-based catheter. *Mechanical Systems and Signal Processing*, *154*, 107532. https://doi.org/10.1016/j.ymssp.2020.107532

Takosoglu, J. (2020). Angular position control system of pneumatic artificial muscles. *Open Engineering*, *10*(1), 681–687. https://doi.org/10.1515/eng-2020-0077

Tran, V. P., Nguyen, T. H. T., Ngo, H. N., Nguyen, M. K., Nguyen, C. N., & Nguyen, C. N. (2023). Position control of a pneumatic artificial muscle using a PID controller. *Can Tho Univ. J. Sci.*, *59*(ETMD), 45–49. https://doi.org/10.22144/ctu.jvn.2023.028 (in Vietnamese).

Tsai, T.-C., & Chiang, M.-H. (2023). A Lower Limb Rehabilitation Assistance Training Robot System Driven by an Innovative Pneumatic Artificial Muscle

System. *Soft Robotics*, *10*(1), 1–16. https://doi.org/10.1089/soro.2020.0216

Vo, C. P., & Ahn, K. K. (2022). An Adaptive Finite-Time Force-Sensorless Tracking Control Scheme for Pneumatic Muscle Actuators by an Optimal Force Estimation. *IEEE Robotics and Automation Letters*, *7*(2), 1542–1549. https://doi.org/10.1109/LRA.2021.3136300

Wang, W., Pang, H., Li, X., Wu, Y., & Song, X. (2022). Research on speed control of permanent magnet synchronous motor based on RBF neural network tuning PID. *Journal of Physics: Conference Series*, *2264*(1). https://doi.org/10.1088/1742-6596/2264/1/012018

Zabihollah, S., Moezi, S. A., & Sedaghati, R. (2024). Development of enhanced force models to analyze the nonlinear hysteresis response of miniaturized pneumatic artificial muscles. *Smart Materials and Structures*, *33*(8). https://doi.org/10.1088/1361-665X/ad6228

Zang, X., Liu, Y., Heng, S., Lin, Z., & Zhao, J. (2017). Position control of a single pneumatic artificial muscle with hysteresis compensation based on modified Prandtl–Ishlinskii model. *Bio-Medical Materials and Engineering*, *28*(2), 131–140. https://doi.org/10.3233/BME-171662

Zhang, X., Sun, N., Liu, G., Yang, T., & Fang, Y. (2024). Hysteresis Compensation-Based Intelligent Control for Pneumatic Artificial Muscle-Driven Humanoid Robot Manipulators With Experiments Verification. *IEEE Transactions on Automation Science and Engineering*, *21*(3), 2538–2551. https://doi.org/10.1109/TASE.2023.3263535

Zorro, J. F., Barrera, Y. C., Viancha, N. N., Totaitive, C. S., & Fernández-Samacá, L. (2022). Design and implementation of a PID controller for a didactic pneumatic levitation system monitored by smartphone. *Automática y Robótica En Latinoamérica. Aportes Desde La Academia*, *October*, 111–126. https://doi.org/10.2307/j.ctv2d6jrr4.9